

Simulating discrete models of pattern formation by ion-beam sputtering

Alexander K Hartmann¹, Reiner Kree² and Taha Yasseri²

¹ Institut für Physik, Universität Oldenburg, 26111 Oldenburg, Germany

E-mail: a.hartmann@uni-oldenburg.de

² Institut für Theoretische Physik, Universität Göttingen, Friedrich-Hund Platz 1, 37077 Göttingen, Germany

E-mail: kree@theorie.physik.uni-goettingen.de,

yasseri@theorie.physik.uni-goettingen.de

Abstract. A class of simple, (2+1) dimensional, discrete models is reviewed, which allow to study the evolution of surface patterns on solid substrates during ion beam sputtering (IBS). The models are based on the same assumptions about the erosion process as the existing continuum theories. Several distinct physical mechanisms of surface diffusion are added, which allow to study the interplay of erosion driven and diffusion driven pattern formation. We present results from our own work on evolution scenarios of ripple patterns, especially for longer time scales, where non-linear effects become important. Furthermore we review kinetic phase diagrams, both with and without sample rotation, which depict the systematic dependence of surface patterns on the shape of energy depositing collision cascades after ion impact. Finally, we discuss some results from more recent work on surface diffusion with Ehrlich-Schwoebel barriers as driving force for pattern formation during IBS and on Monte Carlo simulations of IBS with codeposition of surfactant atoms.

PACS numbers: 05.10.-a,68.35.-p,79.20.-m

Submitted to: *J. Phys.: Condens. Matter*

1. Introduction

The generation of surface patterns by ion beam sputtering (IBS) at low or intermediate ion energies has become a promising tool for nanotechnologies. Since the early observations of self-organized ripple patterns emerging on solid substrates under IBS [1], tremendous improvements in pattern variety and quality have been achieved (for a review see [2]). Nowadays, it is possible to fabricate regularly spaced ripple structures [3] as well as ordered arrays of quantum dots [4] on a wide variety of substrates. The patterns form spontaneously, while the system is driven far from equilibrium by the steady flux of impinging ions. Many of the physical mechanisms underlying this self-organized pattern formation remain poorly understood. Consequently, the unexploited potential of IBS as a fabrication method for nanostructures cannot be assessed systematically and new processing conditions have often led to surprising new results. There are a number of excellent recent reviews of the field available, which cover both experimental findings and theoretical modelings [2, 5, 6]. Here, we will mainly focus on the theoretical approach of (kinetic) Monte Carlo simulations by discussing results, which we achieved during the last years with this method and try to put them into a coherent perspective.

The emerging surface patterns may be classified roughly into three types, according to the dominant mechanism, by which they are formed: *Bradley-Harper ripple structures*, *Ehrlich-Schwoebel structures* and *ordered arrays of regular quantum dots*. They will be briefly introduced in the following. Besides these, there are two more prototypes, which constitute reference patterns for many purposes, and which may also appear during IBS: the *randomly rough surface* and the *smooth or layer-by-layer eroded surface*. The rough surfaces usually exhibit self-affine properties [7].

The formation of periodic ripple structures has been observed experimentally in amorphous materials [8], metallic crystals [9, 10] and semiconductors amorphized by the ion beam [11, 12]. Ripples are typically oriented perpendicular to the projection of the ion beam in the surface plane for small angles of incidence θ (relative to the surface normal), whereas for larger angles θ , the observed ripple pattern is rotated by 90° .

At early times, ripples form and grow exponentially (as the surface roughness does). With increasing ion fluence, at least two stunningly distinct scenarios of evolution appear. Either, a crossover from ripple structures to self-affine, rough surfaces is observed [10], with ripple wavelength and roughness increasing with time as a power law, or the roughness saturates and extremely well-defined, regular ripples appear, which exhibit increasing order up to the longest experimental time scales [3].

Our present, partial understanding of these features is based upon the work of Bradley and Harper (BH) [13], who found that Sigmund's sputtering theory [14] implies a curvature dependence of the sputtering yield. This will lead to a curvature instability, which is stabilized again by surface diffusion at small length scales. The original linear theory of BH was extended into a non-linear continuum theory of surface evolution by sputter erosion, which takes on the form of an anisotropic Kuramoto-Sivashinsky (KS)

equation [15] with additive noise [16, 17, 18]. The linear BH theory should apply to the early stages of pattern evolution, but it fails to predict the observed growth rates quantitatively [19].

To investigate the analytic continuum theory beyond the linearized regime, numerical integrations of the KS equation have been performed [20, 21], which uncovered two markedly different long-time regimes depending on the signs of the non-linear couplings. None of these scenarios, however, is capable of explaining the increase of order observed under some carefully controlled processing conditions.

It is a hallmark of BH ripple structures that they are oriented by the ion beam direction, but in many experiments, especially on single-crystalline, metallic substrates, patterns are observed, which are oriented by the anisotropies of the surface. Such structures may be either ripple-like, dot-like, or hole-like. In many aspects they closely resemble structures observed in molecular beam homoepitaxial (MBE) growth where their emergence has been carefully studied experimentally and theoretically. The common driving force of such structures has been identified as non-equilibrium surface currents, which are due to additional energy barriers against diffusion over step edges (Ehrlich-Schwoebel barriers E_{ES}). These currents provide a net uphill mass transport and thus generate diffusional instabilities, which lead to mound-like structures in MBE. Phenomenological expressions of the Ehrlich-Schwoebel (ES) current have been added to the continuum theory of IBS, but no first principle derivation of the analytic form of these currents is available. To apply the MBE concepts to IBS, it is assumed that IBS creates extra vacancies at the surface, which diffuse like the adatoms, but with a different — usually higher — activation energy. Thus one expects either clustering of vacancies into hole-like structures, or clustering of adatoms into mound-like structures, driven by ES currents. A crossover between BH ripple patterns and ES patterns can be induced by varying the temperature. For high temperatures ($E_{ES} \ll kT$), the ES barriers are ineffective, and for very low temperatures, thermal diffusion is too slow to significantly contribute to the evolution of the surface morphology. Thus ES patterns are expected in an intermediate temperature regime, which has been observed in experiments [2].

A third class of patterns has first been observed on GaSb [4]. It consists of ordered arrays of regularly shaped dots (quantum dots). Meanwhile, similar structures have been found on other binary substrates (InP, InAs) [22, 23], but also on Si [24, 25]. The dots usually form hexagonal lattices, but square lattices have also been observed [23]. The appearance of such structures depends sensitively upon the processing conditions. First they were observed under normal incidence, but subsequently they were found under oblique ion incidence with [23] and also without [26] sample rotation. The type of ordering may change by only slight changes in temperature. The evolution of order of these patterns is characterized by a saturation of roughening and an increase of long-range order and shape regularity with sputtering time, similar to the evolution of the sharp ripples obtained in [3]. These patterns could not be explained within the continuum theory based upon the anisotropic Kuramoto-Sivashinsky model. There are two recent extensions of the continuum model, which are able to produce hexagonally

ordered dots as a generic feature. One of them introduces an ad hoc damping term into the Kuramoto-Sivashinsky equation [27], while the other takes into account an adatom density as a separate variable within a dynamical model built in analogy to hydrodynamic models of aeolian sand dunes [28, 29]. Both models need redeposition as a critical feature. There may be other mechanisms leading to quantum dot arrays. In MBE such structures appear due to elastic stresses, especially in heteroepitaxy. During sputtering erosion the surface layer of a binary compound develops a stoichiometric ratio, which differs from the bulk [30]. Thus misfits may lead to considerable stresses, which have not been included into continuum theories at present. The facilitated generation of quantum dot arrays on Si [31], which is covered by codeposited submonolayer of Mo, also hints at the important role of the interplay between redeposition and binary system dynamics. Recently, this interplay has been studied more systematically using a technique, which is called *surfactant sputtering* by Hofss and Zhang [32]. In this setup, the codeposition of submonolayer "surfactant" species can be controlled and gradients of the codeposited density can be generated. Besides useful technical applications, these experiments also constitute a good testing ground for models involving binary adatom layers.

Given the incomplete understanding of the physical mechanisms of surface pattern formation by IBS, computer simulations may be particularly helpful, especially if combined with results from continuum theory and compared to experimental findings. Two types of simulations have been performed up to now. Koponen et al [33, 34] calculated collision cascades emerging from single ion impact within the binary collision approximation. They find ripples in accordance with linearized BH theory [34] which appear both with and without additional surface relaxation processes. This indicates the presence of an ion-induced surface diffusion mechanism, which has also been predicted from BH [18]. The simulations did not yet reach time scales where the non-linear effects of the continuum theories could be analyzed. On the other hand, scaling properties of the roughness of ion-irradiated surfaces have also been investigated within this approach [33]. In a different approach, Cuerno et al [35] proposed a simple, discrete stochastic model with an update rule, which incorporates the θ -dependence of the sputtering yield and a simple curvature dependence of the erosion probability *ad hoc*. Within this model, it is possible to study the crossover from ripples to rough surfaces during the evolution of an irradiated 1-dimensional system. This approach has been extended to 2-dimensional systems and to kinetic Monte Carlo simulations [19, 36, 37, 38, 39, 40, 41], which also take into account surface diffusion processes. In this paper, we review results we obtained [38, 39, 40, 41] with such discrete models, as well as some recent and as yet unpublished results from our work.

The advantages of discrete Monte Carlo simulations nicely complement the advantages of continuum approaches. MC models may be designed, which are based on exactly the same assumptions as BH theory and its extensions [38]. Thus it is possible to check predictions of continuum expansions and identify artifacts, which only result from the truncation of the expansion. Even more important is the fact that non-

equilibrium surface currents are modeled quasi-atomistically by energy barriers, which can be calibrated by independent experiments, whereas continuum theories have to use phenomenological forms of such currents. Furthermore, the flexibility of MC modeling makes it easy to include new mechanisms, like codeposition, for example. On the other hand, a kinetic MC simulation does only have access to a limited range of time- and length-scales, which may not cover all the parameter regions of experimental interest.

In the following, we first introduce our simulation models and discuss scenarios of the evolution of ripple patterns. Then we review results on kinetic phase diagrams, which describe the dependence of patterns on the shape of the collision cascade after ion impact, as described by the Sigmund formula [13, 14]. In particular we will compare patterns on rotated samples with patterns emerging under identical processing conditions on non-rotated samples. In the next section we demonstrate that the crossover from erosion driven to diffusion driven pattern formation can be studied by Monte Carlo simulations. Finally we present first results on Monte Carlo simulations of IBS with codeposition of surfactant atoms, which has recently been introduced as a new and promising variant of controlled pattern formation by IBS [32].

2. Kinetic Monte Carlo Simulation

We study lattice systems of size $L \times L$ with periodic boundary conditions. The material surface is defined by a time-dependent discrete height function $h(x, y, t)$ [(2+1) D solid-on-solid (SOS) model]. Hence, this can be interpreted as a simple-cubic lattice of atoms, or as simply columns of “blocks” piled on each other. For all simulations described here, we start with a surface which is initially flat, i.e. $h(x, y, 0) = \text{const.}$ Rough or pre-structured surfaces are implemented very easily.

We have included surface defect creation via sputtering and surface defect motion via diffusion. Each simulation step consists of the sputtering generated by one ion and a certain number of diffusion steps. The simulation time is measured in terms of these steps and corresponds to the fluence in experiments.

2.1. The Sputtering Process

According to Sigmund’s sputtering theory [14], the rate at which material is removed from a solid surface through the impact of energetic particles, is proportional to the power deposited there by the random slowing down of particles. The average energy $E(\mathbf{r}')$ deposited at surface point $\mathbf{r}' = (x', y', -z')$ is given by the Gaussian distribution

$$E(\mathbf{r}') = \frac{\epsilon}{(2\pi)^{3/2}\sigma\mu^2} \exp\left(-\frac{(z'+d)^2}{2\sigma^2} - \frac{x'^2 + y'^2}{2\mu^2}\right). \quad (1)$$

Here we have used a local Cartesian coordinate system with origin at the point of penetration and with the z axis coinciding with the ion beam direction. $d_{\parallel} = z' + d$ is the distance of the surface point from final stopping point of the ion, measured along the ion trajectory, $d_{\perp} = \sqrt{x'^2 + y'^2}$ is the distance perpendicular to it; σ and μ are the

widths of the distribution parallel and perpendicular to the ion trajectory, respectively; ϵ is the total energy deposited, d is the average depth of energy deposition. Sigmund's formula is the basis for *nearly all* theoretical treatments and analysis of experimental results so far, although it may not correspond to the actual form of energy deposition. We have performed [42] binary collision simulations to find a model for $E(\mathbf{r}')$ that is closer to the physical reality. Although this model differs from Sigmund's formula in several qualitative and quantitative aspects, we found that the formation of ripples due to a curvature dependent yield remains a stable feature.

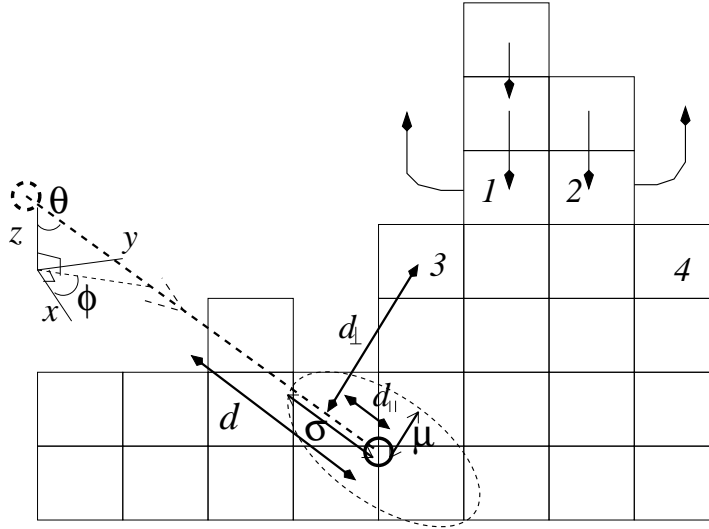


Figure 1. Sketch showing the collision cascade ellipsoid, as described in the text. Erosion may take place from horizontal parts of the surface (atoms at position 3 or 4) or from vertical parts of the surface (atoms at position 1 or 2). The latter has to be followed by surface relaxation steps as indicated to ensures the SOS condition

In [38], we proposed to simulate the sputtering process by applying the Sigmund formula (1) to each single-ion impact. An ion starts at a random position in a plane parallel to the plane of the initially flat surface ($x - y$ plane), and follows a straight trajectory inclined at angle θ to the normal of this plane. The azimuthal angle ϕ describes the orientation relative to the x axis of the ion-beam projection onto the $x - y$ plane. The ion penetrates the solid through a length d and releases its energy, such that an atom at a position $\mathbf{r} = (x, y, h)$ is eroded (see Fig. 1) with probability proportional to $E(\mathbf{r})$. It should be noted that, consistent with the assumptions of the continuum models [5, 13, 16], this sputtering model assumes no evaporation, no preferential sputtering of surface material at point of penetration, no redeposition of eroded material and no creation of extra adatoms from the bulk (the last two constraints have been lifted in the extended continuum theory [28, 29]). The erosion must be implemented in a way, which respects the solid-on-solid assumption, i.e. the surface height must evolve as a single valued, discrete function $h(x, y, t)$. For our initial projects [38, 39], we only allowed particles at the top of a column to be sputtered away, meanwhile we extended the

sputtering model and included erosion from vertical parts of the surface as well (i.e. atoms marked “1” and “2” in Fig. 1). The time t is measured in terms of the ion fluence; i.e, number of incident ions per two-dimensional lattice site (x, y) . Incidence angle θ , and azimuthal angle ϕ can be adjusted to the actual geometric situation which is to be modeled. The parameters d, σ and μ , which are energy and material dependent, can be obtained by SRIM [43]. For the simulations in [38, 39, 40, 41], we have put ϵ to be $(2\pi)^{3/2}\sigma\mu^2$, which leads to sputtering yields $Y \simeq 7.0$, which should be kept in mind when comparing simulation results to experimental data. According to the Bradley Harper theory, the ripple wavelength λ scales like $\lambda \sim Y^{-1/2}$ so that lower yields lead to correspondingly larger length scales.

2.2. Modeling Surface Diffusion

During our studies, we have used different models to describe the surface motion of atoms. These range from simple, irreversible surface relaxation to activated hopping over energy barriers, which may depend both on initial and final state of the move and include ES barriers. We always use full diffusion models, so one diffusion step refers to a complete sweep of the lattice. In the following, we briefly introduce the three basic types of diffusion models, which we have used throughout our simulations.

The first is a simple non-thermal irreversible surface relaxation introduced by Wolf and Villain [44]. For each column, it is tested once during a sweep, whether the particle at the top of the column can increase its coordination number, i.e. its number of nearest neighbors, by hopping to a neighboring column. If this is the case, the particle hops to that neighbor column where it obtains the highest coordination number. This model corresponds to an irreversible downhill relaxation of the energy, if each nearest neighbour contributes a fixed bonding energy. It may be dominant at low enough temperatures because surface configurations with a very high energy (a single column of atoms without nearest neighbours, for example) are most probably locally unstable and can be left without crossing any energy barrier.

The second model [45] is based on the assumption that the diffusion process is determined by the Hamiltonian, which also controls the thermal roughening of a facet on the surface. For each step, a site i and one neighbor site j are randomly selected. The trial move is an atom hopping from i to j , i.e. $h_i = h_i - 1$ and $h_j = h_j + 1$. We calculate the surface energy before and after the hop using the energy function

$$E = \frac{J}{2} \sum_{\langle i,j \rangle} |h_i - h_j|^n. \quad (2)$$

J is a nearest neighbor coupling constant and h_i is the height variable at site i . The summation extends over nearest neighbor pairs. We have used $n = 2$ in our simulations, which implies higher barriers for uphill hops and for hops approaching a step edge on an uphill terrace than for detachment from step edges and reproaching from a step edge on an uphill terrace, respectively.

The hop is allowed with the probability

$$p(i \rightarrow f) = 1/\left[1 + \exp\left(\frac{E(i \rightarrow f)}{k_B T}\right)\right] \quad (3)$$

where $E(i \rightarrow f)$ is the energy difference between the initial and final states of the move. T is the substrate temperature, and k_B is the Boltzmann constant.

The third (“Arrhenius”) model is based on a kinetic MC procedure. For each step, a move from initial (i) to final (f) configuration is chosen randomly from a predefined list. Here we restrict moves to nearest neighbour hops from site i to site f , but we have to include more moves, if we want to model material specific diffusion processes. The move is performed with a probability proportional to an Arrhenius hopping rate

$$k = k_0 \exp\left(-\frac{E(i \rightarrow f)}{k_B T}\right) \quad (4)$$

$k_0 \sim 2k_B T/h$ is the vibrational frequency of a surface adatom, i.e. a hopping attempt rate, h being Planck’s constant. Values of the energy barriers $E(i \rightarrow f)$ have to be taken from experimental or simulation data. In the simplest case, the binding energy of an adatom is the sum of interaction energies E_{NN} with its nearest neighbours (bonds), and the total binding energy is identified with the energy barrier, so that $E(i \rightarrow f) = E_{NN} * (\text{number of nearest neighbour atoms})$. As a slight generalization, one may assume that the bond of an adatom to a substrate atom contributes a different energy $E_S \neq E_{NN}$, in which case $E(i \rightarrow f) = E_S + E_{NN} * nn(i)$, where $nn(i)$ denotes the number of in-plane nearest neighbour atoms of site i . In these models, the barriers only depend upon the initial state i and are determined by the number of bonds, which have to be broken to leave i . They are referred to as *bond breaking models*. Note that in these models, the energy barrier for diffusion along a step edge is the same as that for detachment from the step edge. Furthermore the diffusion of an isolated adatom (barrier E_S) is much smaller than for an isolated surface vacancy (barrier $E_S + 3E_{NN}$). For many materials this is a poor representation of the physical reality, but the model has the advantage of using only 2 parameters, which have to be calibrated. Therefore we use it as a generic model in cases, where diffusion only smoothens the surface and leads to a wavelength selection of BH ripples.

In a more refined modeling, energy barriers may depend both on initial and final state of a move (referred to as *Kawasaki-type barriers*, in analogy to the Kawasaki dynamics of Ising systems). For our simulations we use two types of such barriers:

- *net bond breaking barriers*: $E_{nb}(i \rightarrow f) = \max\left(0, (nn(i) - nn(f))E_{NN}\right)$
- *ES barriers*:

$$E_{ES}(i \rightarrow f) = \begin{cases} E_{ES} & \text{if } f \text{ is in plane with } i \text{ and} \\ & \text{at the upper edge of a step} \\ 0 & \text{otherwise} \end{cases}$$

Default values used in many of our simulations are $E_{ES} = 0.15\text{eV}$ for the ES barrier, a substrate term $E_S = 0.75\text{eV}$ and a nearest neighbor bonding of magnitude $E_{NN} = 0.18$

eV. Temperature is measured in units of eV k_B^{-1} ($T \simeq 0.025eVk_B^{-1}$ corresponds to room temperature 300 K). Hence, the hopping attempt rate k_0 is $\sim 10^{12} \dots 10^{13} s^{-1}$, with a correspondingly low hopping probability resulting from Eq. 4, which would slow down the simulation. Thus we incorporate the factor $\exp(-E_S/k_B T)$ into a rescaled attempt rate k_1 such that the hopping rate reads

$$k = k_1 \exp\left(-\frac{\Delta E}{k_B T}\right) \quad (5)$$

where $k_1 = k_0 \exp\left(-\frac{E_S}{k_B T}\right) \ll k_0$ and $\Delta E = E_{nb}(i \rightarrow f) + E_{ES}(i \rightarrow f)$. The comparison of this attempt rate to the ion current density used in experiments, determines the ratio between the number of sputtering steps and the number of surface diffusion steps made in the simulation. Note that for isolated atoms on plane terraces, which are far from down steps, $\Delta E = 0$, i.e. each hop is accepted independent of the temperature.

To set time-scale and temperature related parameters, consider, as a typical example, a system with $N = 10^{15}$ atoms/cm² at the surface. Since typical experimental ion current densities are of the order $F = 7.5 \times 10^{14}$ ions/(cm²s), this implies a flux of $\Phi = F/N \simeq 0.75$ ions/(atom s). From the values given above, we get default hopping attempt rates k_1 of around $100 s^{-1}$ for temperatures around $350 K$, hence 100 sweeps of the diffusion mechanism correspond to 0.75 ions per surface atom. Thus, we would initiate a diffusion step (one sweep over the lattice) every $\Phi L^2/k_1 = 0.0075 L^2$ erosion steps. To study crossover from erosion to diffusion driven pattern formation, we will increase this default rate by factors up to 10^3 in Sect. 6

3. Typical pattern evolution scenarios of BH ripples

The MC models described above are capable of reproducing many salient features of IBS patterns observed in experiments. A typical scenario of surface evolution with smoothing surface diffusion and angle θ below a critical threshold has been discussed by Monte Carlo simulations in Ref. [38]. It starts as depicted in the upper row of Fig. 2. At short times, the surface roughens. Then ripples perpendicular to the $x - y$ projection of the ion-beam are formed. The further evolution, however, strongly depends upon the surface diffusion. For thermodynamic diffusion and for Arrhenius diffusion mechanisms at temperatures, where ES barriers are not a dominant pattern forming mechanism, the ripples propagate slowly, coarsen, and, due to the increasing influence of non-linear effects, typically disappear at longer times, see Fig. 3 (left panel). The orientation of the ripples is rotated by 90° if θ exceeds some critical value, similar to many experiments and to the results of linear continuum theory. The long-time behavior, where the ripples have disappeared, has been studied to some extent in Ref. [38].

For intermediate times, where the ripples coarsen, we found that the ripple wavelength increases with time. For the Arrhenius diffusion, the ripple wavelength as a function of time displays a power law increase, similar to results in experiments [46]. The value of the exponent seems to be non-universal. Power law coarsening behaviour

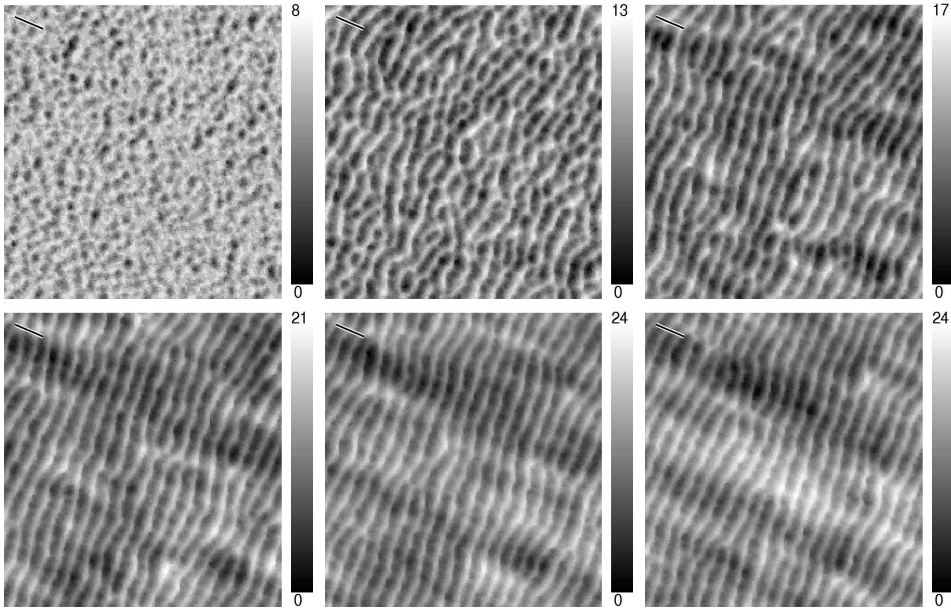


Figure 2. Surface profiles ($L = 256$, $\theta = 50^\circ$, $\phi = 22.0^\circ$, $d = 6.0$, $\sigma = 3.0$, $\mu = 1.5$, Kawasaki-type diffusion with default values for barriers) at a substrate temperature of 600 K and at different times. Starting from top-bottom, left-right, $t=0.5, 1.5, 4.0, 8.0, 12.0$ and 18.0 ions/atom. Ion beam direction, indicated by the bar, is perpendicular to ripple orientation. The scales show the surface height measured from the minimal height of the surface profile.

has also been observed in a number of experiments [2] with varying values for the exponent. We have also found stronger (super-power law) increases (within our second model of surface diffusion) and weaker (supra-power law) increases (when doubling the temperature for the Arrhenius diffusion) in our simulation, but given the time intervals accessible in simulations and in experiments, it is hard to draw conclusions regarding a comparison with experimental results.

We have also studied the propagation velocity of the ripples by means of clustering algorithms, i.e. crests of ripples are defined as connected components of columns, where the height is significantly larger [39] than the average height. We observed that the ripple velocity obeys a power-law decrease with increasing time. This again compares qualitatively to experiments [46], but the value of the exponent seems again to be non-universal.

The coarsening and vanishing of ripples is, however, not the only scenario we observed. Fig. 3 shows results of simulations for longer times. The above described scenario with strong and smoothing surface diffusion develops into patterns depicted in Fig. 3 (left). Fig. 3 (middle) shows the pattern under Arrhenius diffusion as in Fig. 2, but after 400 ions/atom. Here, the roughness saturates (note the grey scale of height in the figures) and the ripples develop towards increasing order, i.e. the number of defects reduces. Note that the defect free ripple pattern is still oriented perpendicular to the projected ion beam direction. Using an irreversible Wolf-Villain surface relaxation, [38]

(see Fig. 3 (right)), the patterns evolve towards increasingly sharp and ordered ripples. The orientation of these ripples is, however, tilted ($\approx 17^\circ$) with respect to the projected ion beam direction. These scenarios, which appear if surface motion is dominated by non-equilibrium diffusion currents, are reminiscent of the ripples observed in [3]. Tilted ripples have also been found as an asymptotic scenario within the anisotropic Kuramoto-Sivashinsky equation in [20], but a scenario with long-term, highly-ordered ripples, which do not change their orientation could not be explained within this continuum theory.

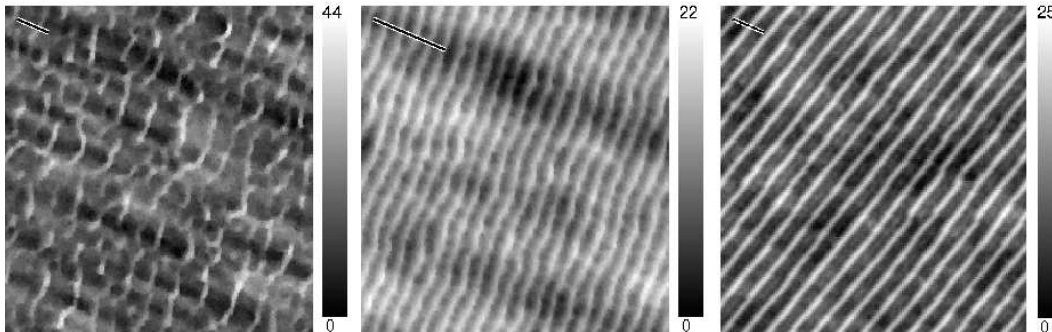


Figure 3. Long time surface evolution. *left*: high temperature $T=0.2$ eV leads to strong, smoothing diffusion in Arrhenius and thermodynamic model. After 20 ions/atom ripple patterns are nearly destroyed; *middle*: Arrhenius diffusion at $T=600$ K for 400 ions/atom. Continuation of the evolution in Fig. 2. Highly ordered and stable ripple patterns develop. *right*: Wolf-Villain type diffusion for $t \approx 10^4$ ions/atom, extremely ordered ripple patterns with tilted orientation. For all three panels $L = 256, \phi = 22^\circ, \theta = 50^\circ$

4. Dependence of patterns on ion energy distribution

In general, the evolution of patterns depends upon all the processing conditions, for example on substrate, ion energy, temperature and geometric parameters of the setup. The parameter space is much larger than what can be explored by experiments in feasible time, so one concentrates on easily controllable parameters, which are expected to have significant influence on the pattern formation. One such parameter is the temperature, which controls the competition between the BH mechanism and ES currents as main driving forces for pattern formation. The above sketched crossover scenario between BH and ES patterns has been confirmed by combining data from a number of experiments [2].

In MC simulations, we can vary all the parameters with ease and therefore we can study parts of the parameter space, which are hard to access experimentally. As an example, we exhaustively studied the short and medium time behavior of surface evolution as a function of the energy-distribution parameters μ and σ of equation (1). We have studied about 50 different (σ, μ) combinations ($L = 128, \theta = 50^\circ, \phi = 22^\circ$) using Arrhenius diffusion with bond breaking term and ES barrier of $0.15eV$ at a high

temperature, $k_B T = 0.1\text{eV}$, to avoid a too strong driving force from E_{ES} . We observed six different types of qualitative behavior, corresponding to six different regions in the (σ, μ) space. In Fig. 4 these six regions are indicated for $t = 3$ ions/surface atom at which almost all the surface topographic features are distinct; the corresponding profiles are shown in Fig. 5. The boundaries shown in this sketch do not represent abrupt transitions from one topography to another. Rather we observe a smooth crossover from one behavior to the other. For this reason, we have not used straight lines to represent them in the diagram. Also, we have focused on a typical time $t = 3$, corresponding to timescales often used in experiments, which exhibit a rich behavior as a function of the straggling parameters μ and σ . Only one systematic change of the boundaries occurs with time, which is described below. Finally, although the results collected in Fig. 4 were obtained at $\theta = 50^\circ$, similar “kinetic phases” also occur at other values of θ , with slight deviations at the boundaries.

We performed SRIM simulations [43] to map the kinetic phase diagram (Fig. 4) to experimental setups. The following list is just to give a few examples. Region V: $1.5 - 1.7\text{keV}$ neon(Ne)-ion sputtering of copper(Cu); $1.2 - 1.4\text{keV}$ Ne-ion sputtering of germanium(Ge). Region IV: $650 - 800\text{eV}$ Ne-ion sputtering of silicon(Si). Region III: $800\text{eV} - 1.1\text{keV}$ Ar-ion sputtering of silicon(Si); $550 - 700\text{eV}$ Ne-ion sputtering of C. Note that for most materials and parameter combinations $\sigma \leq \mu$, hence the region V might be difficult to access. Also, SRIM simulations reveal that very large σ and μ , i.e, beyond the values considered here, are impractical, since they can only occur for a higher d . Whereas, the value of d is itself restricted by the range of ion energies that lead to ripple formation.

The following features distinguish the different topographies in Fig. 5:

Region I: rough surface [see Fig. 5(I)] which, as time increases, evolves to a hole topography. The *sizes* of the holes grow and finally coalesce to a ripple topography at long times (see Ref. [40]).

Region II: holes are already prominent in this region [see Fig. 5(II)]; here the *number* of holes increases with time, and again ripples are formed at long times, but at an earlier time than as in region I (not shown as separate figure).

Note that the number of holes decreases [40] with increasing the sputtering depth d . On the other hand, if we vary θ , the number of holes increases [40] with increasing θ . Ripples can be formed here at this time ($t=3$) if θ is increased beyond $\theta_r(t=3) \simeq 60^\circ$.

Region III: the ripple phase [38, 39]. Having observed in regions I and II that holes evolve into ripples with time, we studied this region from the very earliest times ($t=0-3$) but found only very tiny holes, i.e not as pronounced as in region II, in the course of ripple formation. Thus, comparing regions I,II and III, there seem to be two different processes of ripple formation. Ripples can be formed quickly by evolving directly from a slightly rough surface, or they can be formed slowly via the creation of holes, which coalesce to ripples on longer time scales. Note that in regions I and II, the resulting ripple wavelength is smaller than the size of the holes generated on smaller time, while in region III the ripple wavelength is larger than the tiny holes.

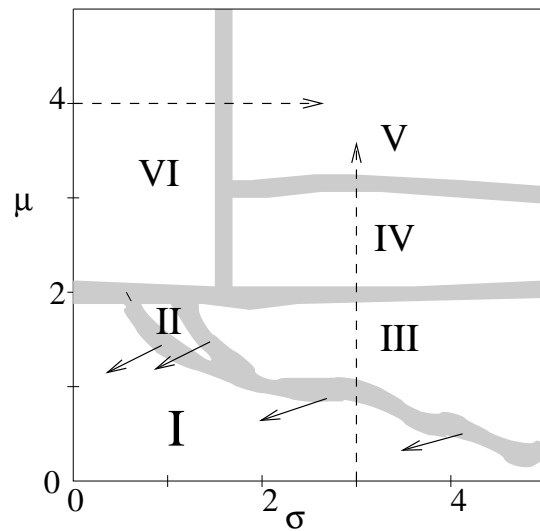


Figure 4. Different topographic regions ($\theta = 50^\circ$, $d = 6$). Region I: rough surface; II: holes; III: clear ripples oriented perpendicular to ion beam direction; IV: short ripples (resulting from increased μ); V: dots; VI: non-oriented structures. The short arrows indicate the evolution of the boundaries between different regions with respect to time. Hence, region III grows at the expense of region I, while region II describes only a short transient.

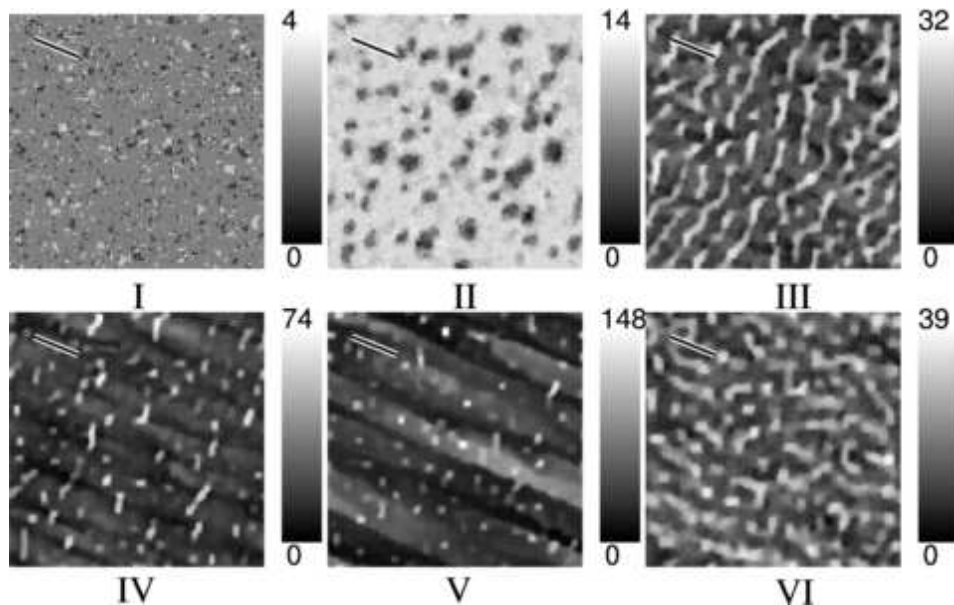


Figure 5. Profiles for parameters chosen from each topographic region in Fig. 4; $\theta = 50^\circ$, $d = 6$, $t = 3.0$. (I) $\sigma = 1$, $\mu = 0.5$; (II) $\sigma = 1$, $\mu = 1.5$; (III) $\sigma = 3$, $\mu = 1.5$; (IV) $\sigma = 4$, $\mu = 2.5$; (V) $\sigma = 5$, $\mu = 5$; (VI) $\sigma = 0.5$, $\mu = 5$. The bar, on all profiles, denote the ion beam direction

To summarize the dynamical behavior observed in regions I-III, for long (but not infinite) times ripples are formed everywhere, but region III grows on the expense of the two other regions. Region II represents only a short transient behavior. It might extend further to larger values of σ in a very narrow range between region I and III, but we cannot resolve this with our limited number of parameter combinations. Please note that at very long times, beyond the usual time scales accessible in standard experiments, nonlinear effects become more important and the ripples coarsen and disappear again [38, 39].

Region IV: consists of a mixture of dots and short ripples, which eventually give way to the dot “phase” (region V), as σ is increased. Hence, this region seems to “interpolate” between regions III and V.

Region V: consists of dots. These dots are formed on some ripple-like structures oriented perpendicular to the ion beam direction, as discussed below in more detail. Noting that our model is a solid on solid model on a square lattice, the dots are not unsimilar to the QDs predicted by theory [47, 48] and observed in experiments [4, 24].

Region VI: consists of non-oriented structures exhibiting a typical length scale, but only a slight orientation preference parallel to the ion beam. This region, as mentioned above, is probably difficult to access in experiments.

More results about this phase diagram, including time-dependence, can be found in Ref. [40].

5. Patterns on rotated samples

Substrate rotation is a special processing condition considering of increasing technological interest, since quantum dots can be generated [4] in this way.

We have included rotations in our MC simulations [41] by choosing a random azimuthal angle ϕ for each impinging ion, which corresponds to a rotation, which is much faster than the anisotropic pattern forming processes. As seen from Fig. 6 (and Fig. 7, see below), no anisotropy can be found with substrate rotation, as expected from the continuum theory. The ripple structures obtained for $\mu \leq 2$ (Region III of Fig. 5) do not appear for rotated substrates. The underlying parallel ripples of the dot region (Region V of Fig. 5) are also absent for rotated substrates. However, hole formation is not suppressed, we get holes with as without rotation, as it is visible in Fig. 5. This fact can be understood [40] from the continuum theory, which predicts roughly equal erosion rates along both directions for parameters in the hole region, hence there is no anisotropy to be destroyed. Furthermore, ripple patterns perpendicular with respect to the ion beam direction are replaced by non-oriented structures, and the ordered parallel ripples are no longer present if the substrate is rotated (see Fig. 6).

For a closer inspection, we calculate the structure factors, $S(\mathbf{k}, t) = |h(\mathbf{k}, t)|^2$ from the Fourier transform $h(\mathbf{k}, t)$ of the height field $h(\mathbf{r}, t)$. In particular we consider four prototypical topographies marked by letters S, H, N, D in Fig. 6. S stands for “relatively smooth”, H for “hole”, N for “non-oriented structures”, and D for “dots”. The results

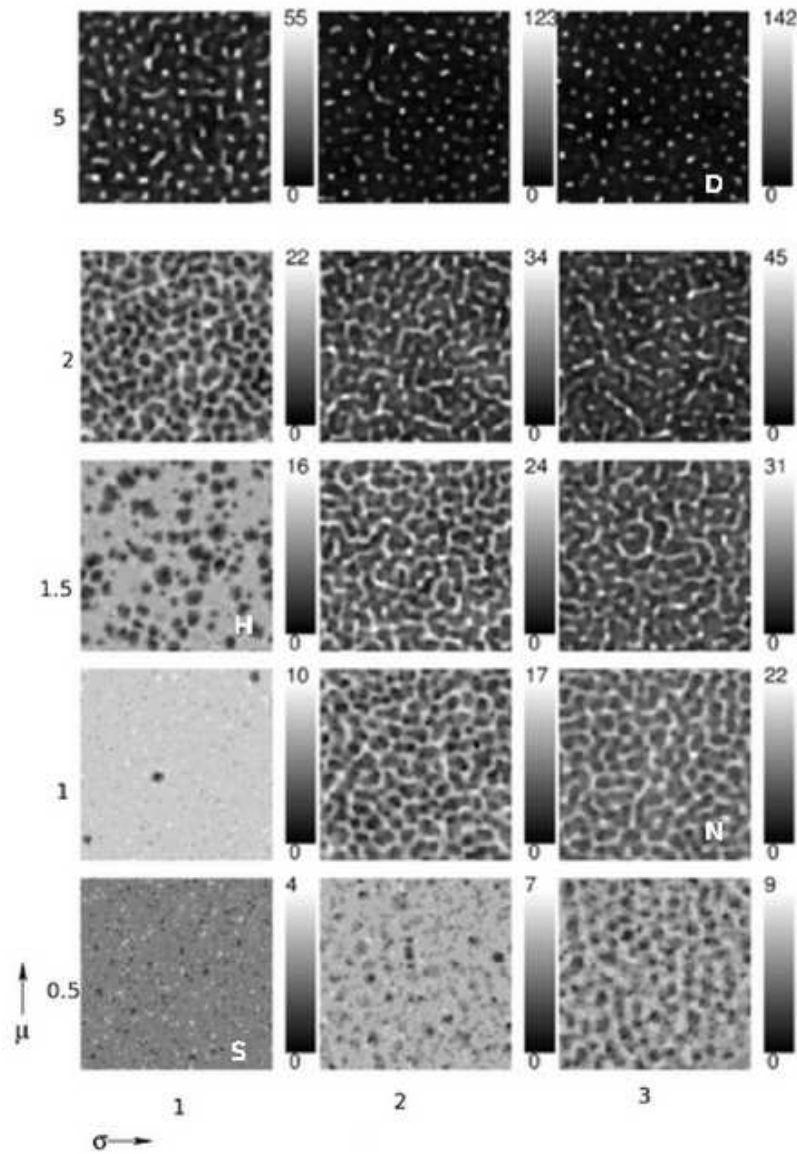


Figure 6. Profiles obtained from simultaneous sputtering and rotation, using the same parameters as in Fig. 5. $t = 3$, $d = 6$, $\theta = 50^\circ$. Left - right columns: $\sigma = 1, 3$, and 5 , respectively. Bottom row - top row: $\mu = 0.5, 1, 1.5, 2$, and 5 , respectively. The last two profiles of the top row belong to the dot region (region V) of Ref. [40]. Structure factors of the lettered profiles are provided in Fig. 7 [S - (relatively) smooth; H - hole; N - non-oriented structures; D - dot].

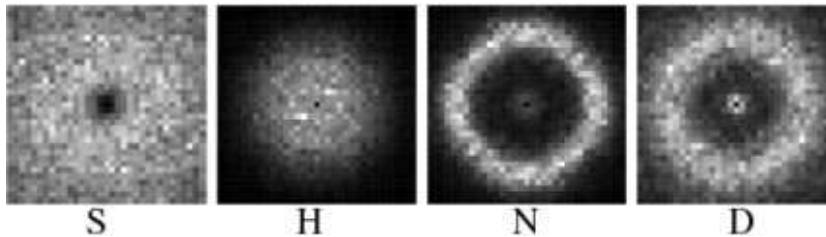


Figure 7. Structure factor of the lettered surface profiles in Fig. 6. S \Rightarrow (relatively) smooth; H \Rightarrow hole; N \Rightarrow non-oriented structures; D \Rightarrow dot.

are shown in Fig. 7. As can be seen from this figure, and as expected, there is no anisotropy visible in all cases. In the case of the relatively smooth surface S, there is also no characteristic length scale. For the hole topography, H, there is still no specific length scale but there now exists an upper bound k_{ub} on $|\mathbf{k}|$ due to the presence of the holes. On the surface with non-oriented structures (N) a well defined length scale with k_{ub} as well as a lower bound k_{lb} can be found. And finally, in the case of the dot topography (D), we also have a characteristic length scale, but k_{lb} is shorter here than for the N topography, which implies that the average separation of the dots is larger than that of the non-oriented structures, as expected from Fig. 6.

6. Interaction of erosion- and diffusion-driven patterns

The interplay of erosion and surface diffusion is of particular importance for the pattern formation during IBS. Let us first take a look at the $\theta = 0$ case, where no BH ripples are generated. Fig. 8 shows different patterns generated by identical erosion from ions at normal incidence under the action of (a) no surface diffusion, (b) bond breaking diffusion and (c) net bond breaking diffusion at 120 K. (b) and (c) contain an identical (default) ES barrier, but the effectively enhanced diffusivity of surface vacancies leads to clear pyramid and pit structures in (c) with a lengthscale of ≈ 10 lattice constants.

As the Arrhenius rates controlling the surface diffusion may change over several orders of magnitude within usual experimental temperature ranges and a simulation will have to perform correspondingly many diffusion steps per ion impact, slight increases in temperature may easily produce a computational bottleneck. As remarked above, our default values correspond to a rescaled attempt frequency (see equation (5)) of $k_1 \approx 100 \text{ s}^{-1}$ at 350 K, whereas it corresponds to $k_1 \sim 7.5 * 10^3 \text{ s}^{-1}$ for 500 K and $k_1 \sim 3 * 10^6 \text{ s}^{-1}$ for 700 K. A number of previous simulations, which tried to explore pattern evolution under the influence of ES surface diffusion simply add vacancies or adatoms randomly (similar to MBE simulations) and do not create them by sputtering events [49, 50, 51]. This approach misses the morphology dependence of the sputter yield, which is essential for the BH instability. To study the crossover from BH ripples to ES structures we first estimated the minimal diffusion rates, which would create structures from ES currents of a given cluster size or a given distance between clusters,

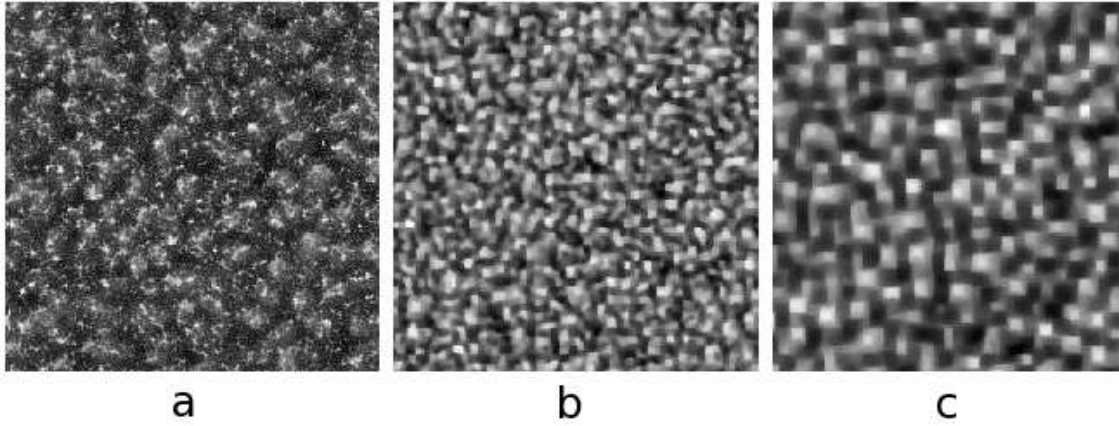


Figure 8. Profiles obtained by normal incidence sputtering with (a) no diffusion, (b) Arrhenius diffusion and (c) Kawasaki diffusion.

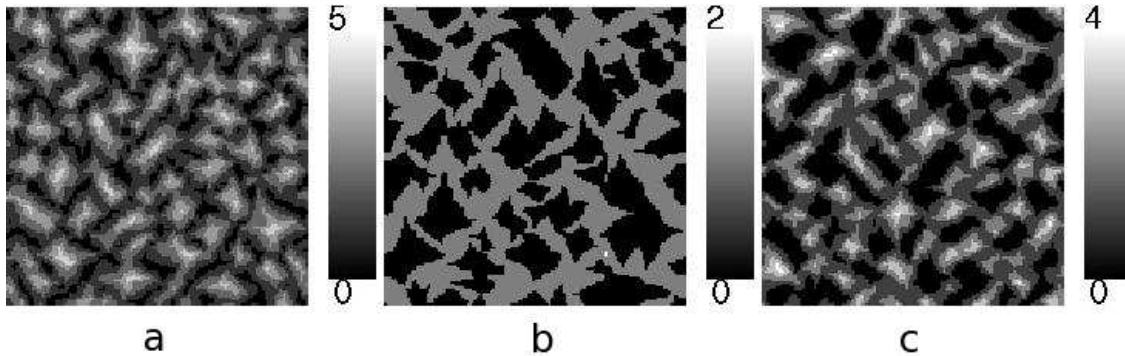


Figure 9. Evolution of clusters formed by (a) ad-atoms, (b) vacancies and (c) ad-atom and vacancies together at $T = 120$ K, $L = 128$, $t = 1.5$ ML. Temperature is chosen such that ES barriers are clearly visible in diffusion currents. k_1 has been increased by a factor of 10^3 with respect to its default value, which corresponds to a decrease in E_S of ≈ 0.069 eV

using well-known arguments from MBE theory [52]. From these estimates, we expect lateral structures of ≈ 10 lattice constants, if we enhance $k_1 = 0.01$ by a factor of $10^3 - 10^4$. Fig. 9 shows patterns with k_1 increased by a factor of 10^3 , resulting from randomly added surface defects. There are clear pyramid or pit structures, which are oriented by crystallographic axes, just as known from MBE simulations.

In Fig. 10 we show the results of a full sputter erosion simulation with 10^3 fold increase in k_1 , at inclined ion beam incidence, with the same average surface defect yield and the same surface diffusion barriers as used in the simulations of Fig. 9. For comparison, we show the result of an identical simulation with default parameters in the left panel of Fig. 10. The difference between the left and right panel can be roughly interpreted as a temperature shift of less than 100 K. Note that pit-and-crest structures replace the usual BH ripples and these structures are partially oriented by the ion beam direction and partially by crystallographic axes. Structures of this type, which

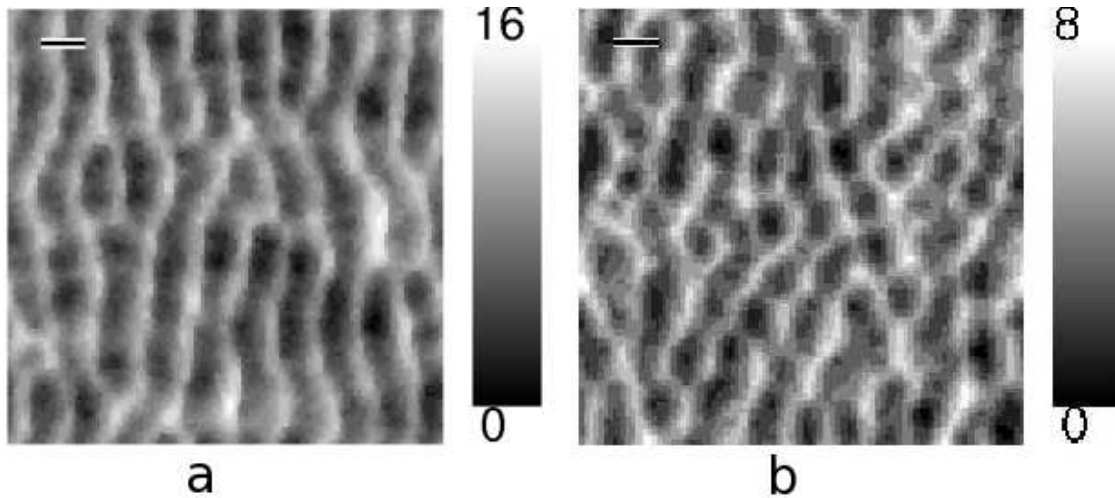


Figure 10. Surface profiles of a system with $L = 128$ for $\theta = 50^\circ$, $\phi =$ (a) 0° at $t = 3ML$. The bar indicates the azimuthal direction of ion-beam. *left*: Arrhenius diffusion with default parameters for bond breaking and ES default parameters, thus $k_1 = 100s^{-1}$, *right*: same as left, but with $k_1 = 10^5s^{-1}$

change significantly under slight temperature changes appear in numerous experimental observations (For reviews see Refs. [2, 6]).

7. Surfactant sputtering

Recently sputter erosion of a monatomic substrate (A) has been combined by codeposition arising from co-sputtering of a nearby target of substrate (B) [32]. Codeposition is adjusted beyond the resputtering limit, so that B atoms form a submonolayer coverage of the A surface with density, which is kept constant and can be carefully controlled. It is also possible to generate gradients of the B coverage in a controlled way. Depending on the surface diffusion of B, on its sputter yield (Y_B), on the induced modification of the A sputter yield (Y_A) and on the mixing and alloying properties of the A-B system, many different pattern forming scenarios can emerge. Here we present some results of MC simulations for simple cases. We restrict the thickness of the B-layer to at most 1 by forbidding diffusional hops, which end on top of B atoms. B atoms, which are sputtered off are replaced by random redeposition. All results shown were obtained at $T = 600$ K (Arrhenius diffusion) after 3 ions/atom. In the model, different binding energies for nearest neighbour pairs (E_{AA} , E_{AB} , E_{BB}) naturally appear. Note, first of all that if $A = B$, the setup is equivalent to an additional long range hopping due to sputtering/redeposition events. Thus patterns should be modified. We find that the ripple wavelength decreases and the surface roughness increases (see Fig: 11 (diamonds)) with increasing coverage. If the sputtering yield of B is increased and at the same time the A yield is suppressed by the presence of B particles as nearest neighbours, the surface roughness decreases as a function of coverage, and very smooth surfaces emerge as shown Fig. 11 (circles).

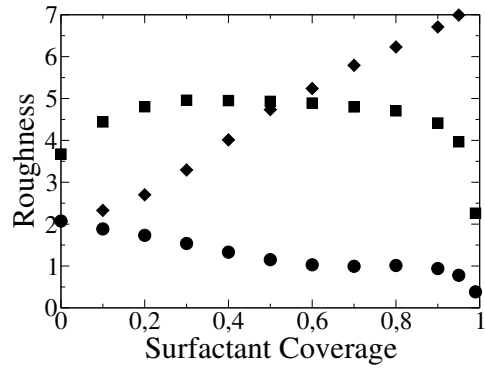


Figure 11. Roughness of surface against coverage with surfactant. *diamonds*: $A=B$, *circles*: Sputtering yield Y_B is $10Y_A$ and the A yield is suppressed by $0.25Y_A$ from every nearest neighbor B atom., *squares*: Clustering of B and demixing favored, $E_{AA} = 0.18$, $E_{AB} = 0$, $E_{BB} = 0.6$. Surface diffusion without ES barriers.

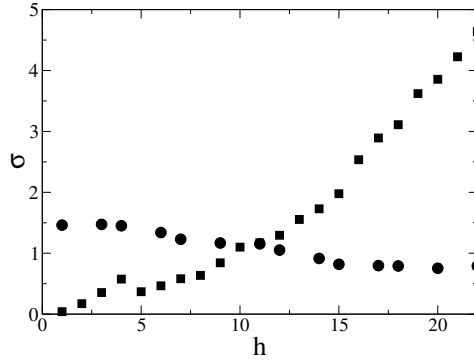


Figure 12. Statistical estimate of surface density of surfactant vs. height. *circles*: substrate species $A =$ surfactant species B , *triangles*: surfactant B is clustering and demixing from A , similar to Ag on Si . Bond energies, see main text.

In Fig. 11 (squares) the barriers have been changed to facilitate B-clustering and favour demixing ($E_{AA} = 0.18$, $E_{AB} = 0$, $E_{BB} = 0.6$, but $E_{ES} = 0$). This causes a highly significant redistribution of the surfactant B on the A surface as is shown in figure 12. The majority of B atoms would be located in valleys of the ripple topography if they were distributed randomly (due to the morphology of the ripples). In the figure, we show the ratio of the number of B atoms to the number of randomly distributed atoms vs. height h , which constitutes a statistical estimate of surfactant surface density. Note that sputtering plus redeposition of $B=A$ atoms only leads to a minor increase of density in valleys, whereas B atoms strongly prefer to assemble on crests of ripples if they cluster and demix from substrate A atoms. This behaviour has been observed in experiments [32] using a Si substrate and Ag surfactant. An improved control of this clustering could open up a way to efficiently fabricate regular arrays of quantum wires.

Surfactant sputtering is also an interesting tool for nanofabrication of profiles [32]. This is demonstrated in Fig. 13, which shows the surface profile emerging from a

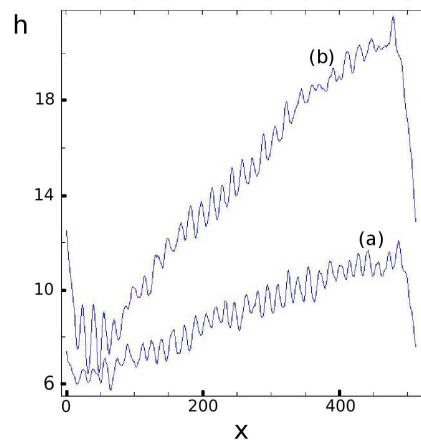


Figure 13. Mean of surface height in direction perpendicular to ion beam direction. In (a) $\lambda_2 = 0$. In (b) $\lambda_2 = 0.25$. In both cases $\lambda_1 = 10$. Average coverage of surfactants is 20 %.

gradient of surfactant density. Note that only a tiny submonolayer coverage results in a rippled topography with nanometer wavelength and well defined slope over micrometer lengthscales.

8. Acknowledgments

The authors would like to thank R. Cuerno, M. Feix, U. Geyer, H. Hofsäss, M. Koelbel, K. Lieb, J. Muñoz-García, M. Uhrmacher and E. Yewande for fruitful collaborations on this subject, many helpful discussions and useful suggestions. This work was funded by the DFG (*Deutsche Forschungsgemeinschaft*) within the SFB (Sonderforschungsbereich) 602 and by the *VolkswagenStiftung* (Germany) within the program “Nachwuchsgruppen an Universitäten”.

References

- [1] M. Navez, C. Sella, and C. Chaperot. *Compte. Rend.*, 254:240, 1962.
- [2] W. L. Chan and E. Chason. *J. Appl. Phys.*, 101:121301, 2007.
- [3] B. Ziberi, F. Frost, T. Höche, and B. Rauschenbach. *Phys. Rev. B*, 72:235310, 2005.
- [4] S. Facsko, T. Dekorsy, C. Koerdts, C. Trappe, H. Kurz, A. Vogt, and H. L. Hartnagel. *Science*, 285:1551–1553, 1999.
- [5] M. A. Makeev, R. Cuerno, and A. L. Barabási. *Nucl. Instr. and Meth. in Phys. Res. B*, 197:185, 2002.
- [6] U. Valbusa, C. Boragno, and F. Buatier de Mongeot. *J. Phys.: Condens. Matter*, 14:8153–8175, Jan 2002.
- [7] E. A. Eklund, R. Bruinsma, and J. Rudnick. *Phys. Rev. Lett.*, 67(13):1759–1762, Sep 1991.
- [8] T. M. Mayer, E. Chason, and A. J. Howard. *J. Appl. Phys.*, 76:1633, 1994.
- [9] S. Rusponi, G. Costantini, C. Boragno, and U. Valbusa. *Phys. Rev. Lett.*, 81(19):4184–4187, Nov 1998.

- [10] S. Habenicht, W. Bolse, K. P. Lieb, K. Reimann, and U. Geyer. *Phys. Rev. B*, 60(4):R2200–R2203, Jul 1999.
- [11] G. W. Lewis, M. J. Nobes, G. Carter, and J. L. Whitton. *Nucl. Instrum. Methods*, 170:363–369, 1980.
- [12] E. Chason, T. M. Mayer, B.K. Kellerman, D. T. McIlroy, and A. J. Howard. *Phys. Rev. Lett.*, 72(19):3040–3043, May 1994.
- [13] R. M. Bradley and J. M. E. Harper. *J. Vac. Sci. Technol. A*, 6:2390–2395, 1988.
- [14] P. Sigmund. *Phys. Rev.*, 184(2):383–416, Aug 1969.
- [15] Y. Kuramoto and T. Tsuzuki. *Prog. Theor. Phys.*, 55:356, 1976.
- [16] R. Cuerno, , and A. L. Barabási. *Phys. Rev. Lett.*, 74(23):4746–4749, Jun 1995.
- [17] M. Makeev and A. L. Barabási. *Appl. Phys. Lett.*, 71:2800, 1997.
- [18] G. Carter. *Phys. Rev. B*, 59(3):1669–1672, Jan 1999.
- [19] E. Chason, W. L. Chan, and M. S. Bharathi. *Phys. Rev. B*, 74(22):224103, 2006.
- [20] M. Rost and J. Krug. *Phys. Rev. Lett.*, 75(21):3894–3897, Nov 1995.
- [21] S. Park, B. Kahng, H. Jeong, and A.-L. Barabási. *Phys. Rev. Lett.*, 83:3486–3489, 1999.
- [22] F. Frost, A. Schindler, and F. Bigl. *Phys. Rev. Lett.*, 85:4116–4119, 2000.
- [23] F. Frost, B. Ziberi, T. Höche, and B. Rauschenbach. *Nucl. Instrum. Methods Phys. Res. B*, 216:9–19, 2004.
- [24] R. Gago, L. Vázquez, R. Cuerno, M. Varela, C. Ballesteros, and J. M. Albella. *Appl. Phys. Lett.*, 78:3316–3318, 2001.
- [25] R. Gago, L. Vázquez, O. Plantevin, J. A. Sánchez-García, M. Varela, M. C. Ballesteros, J. M. Albella, and T. H. Metzger. *Phys. Rev. B*, 73(15):155414, 2006.
- [26] B. Ziberi, F. Frost, and B. Rauschenbach. *Appl. Phys. Lett.*, 87:033113, 2005.
- [27] S. Facsko, T. Bobek, A. Stahl, H. Kurz, and T. Dekorsky. *Phys. Rev. B*, 69:153412, 2004.
- [28] M. Castro, R. Cuerno, L. Vázquez, and R. Gago. *Phys. Rev. Lett.*, 94:016102, Jan 2005.
- [29] J. Muñoz-García, M. Castro, and R. Cuerno. *Phys. Rev. Lett.*, 96(8):086101, 2006.
- [30] V. B. Shenoy, W. L. Chan, and E. Chason. *Phys. Rev. Lett.*, 98:256101, Jun 2007.
- [31] G. Ozaydin, A. zcan, Yiyi Wang, K.F. Ludwig, Hua Zhou, R.L. Headrick, and D.P. Siddons. *Appl. Phys. Lett.*, 87:163104, 2005.
- [32] H. Hofsäss and K. Zhang. *Appl. Phys. A*, (on-line version) 2008.
- [33] I. Koponen, M. Hautala, and O. P. Sievänen. *Phys. Rev. B*, 54(19):13502–13505, Nov 1996.
- [34] I. Koponen, M. Hautala, and O. P. Sievänen. *Phys. Rev. Lett.*, 78(13):2612–2615, Mar 1997.
- [35] R. Cuerno, H. A. Makse, S. Tomassone, S. T. Harrington, and H. E. Stanley. *Phys. Rev. Lett.*, 75(24):4464–4467, Dec 1995.
- [36] M. Stepanova and S.K. Dew. *Appl. Phys. Lett.*, 84:1374, 2004.
- [37] A.-D. Brown, J. Erlebacher, W. L. Chan, and E. Chason. *Phys. Rev. Lett.*, 95:056101, 2005.
- [38] A. K. Hartmann, R. Kree, U. Geyer, and M. Kölbl. *Phys. Rev. B*, 65:193403, 2002.
- [39] E. O. Yewande, A. K. Hartmann, and R. Kree. *Phys. Rev. B*, 71:195405, 2005.
- [40] E. O. Yewande, R. Kree, and A. K. Hartmann. *Phys. Rev. B*, 73:115434, 2006.
- [41] E. O. Yewande, R. Kree, and A. K. Hartmann. *Phys. Rev. B*, 75:155325, 2007.
- [42] M. Feix, A. K. Hartmann, R. Kree, J. Muñoz-García, and R. Cuerno. *Phys. Rev. B*, 71(12):125407, 2005.
- [43] J. F. Ziegeler, J. P. Biersack, and K. Littmark. *The Stopping and Range of Ions in Matter*. Pergamon, New York, 1985. see also <http://www.srim.org/>
- [44] D. E. Wolf and J. Villain. *Europhys. Lett.*, 13:389, 1990.
- [45] M. Siegert and M. Plischke. *Phys. Rev. E*, 50(2):917–931, Aug 1994.
- [46] S. Habenicht, K. P. Lieb, J. Koch, and A. D. Wieck. *Phys. Rev. B*, 65:115327, 2002.
- [47] B. Kahng, H. Jeong, and A.-L. Barabási. *Appl. Phys. Lett.*, 78:805, 2001.
- [48] F. Frost. *Appl. Phys. A*, 74:131–133, 2002.
- [49] O. Malis, J.D. Brock, R.L. Headrick, M.S. Yi, and J.M. Pomeroy. *Phys. Rev. B*, 66:035408, 2002.
- [50] M. V. R. Murty, B. Cowles, and B.H. Cooper. *Surf. Sci.*, 415:328–335, 1998.

- [51] C. Teichert, C. Ammer, and M. Klaua. *Phys. Status Solidi A*, 146:223–242, 1994.
- [52] J. Villain and A. Pimpinelli. *Physique de la croissance cristalline*. Aléa-Saclay-Eyrolles, Paris, 1994.